Available online at www.sciencedirect.com
ScienceDirect
Remote Sensing of Environment 107 (2007) 496–509
Remote Sensing of Environment
www.elsevier.com/locate/rse

Mapping northern land cover fractions using Landsat ETM+

Ian Olthof *, Robert H. Fraser

Natural Resources Canada, Earth Sciences Sector, Canada Centre for Remote Sensing, 588 Booth Street, Ottawa, ON, Canada K1A 0Y7

Received 1 May 2006; received in revised form 5 October 2006; accepted 7 October 2006

Abstract

The goal of fractional mapping is to obtain land cover fraction estimates within each pixel over a region. Using field, Ikonos and Landsat data at three sites in northern Canada, we evaluate a physical unmixing method against two modeling approaches to map five land cover fractions that include bare, grass, deciduous shrub, conifer, and water along an 1100 km north–south transect crossing the tree-line of northern Canada. Error analyses are presented to assess factors that affect fractional mapping results, including modeling method (linear least squares inversion (LLSI) vs. linear regression vs. regression trees), number of Landsat spectral bands (3 vs. 5), local and distant fraction estimation using locally and globally calibrated models, and spatial resolution (30 m vs. 90 m). The ultimate purpose of this study is to determine if reliable land cover fractions can be obtained for biophysical modeling over northern Canada from a three band, resampled 90 m Landsat ETM+ mosaic north of the tree-line. Of the three modeling methods tested, linear regression and regression trees with five spectral bands produced the best local fraction estimates, while LLSI produced comparable results when unmixing was sufficiently determined. However, distant fraction estimation using both locally and globally calibrated models was most accurate using the three spectral bands available in the Landsat mosaic of northern Canada at 30 m resolution, and only slightly worse at 90 m resolution. While local calibrations produced more accurate fractions than global calibrations, application of local calibration models requires stratification of areas where local endmembers and models are representative. In the absence of such information, globally calibrated linear regression and regression trees to estimate separate fractions is an acceptable alternative, producing similar root mean square error, and an average absolute bias of less than 2%.

Keywords: Landsat ETM+; Spectral unmixing; Arctic; Vegetation; Land cover; Fractions; Ikonos

1. Background

Conventional satellite remote sensing land cover maps are based on hard classifiers, where pixels are assigned a single land cover label. In areas that are relatively homogeneous at the level of the minimum mapping unit (MMU) of moderate resolution sensors, single land cover labels may be appropriate. However, depending on the size of objects relative to the MMU and their spatial distribution, pixels may be composed of more than one object type, producing mixed pixels. Land cover legends used to generate a hard classification deal with the mixed pixel problem by including mixed land cover classes. For example, most land cover legends include a mixed forest class composed of both conifer and deciduous land cover classes. Hard classifiers can map forested areas well due to the fact that trees are large objects relative to the MMU, and often occur in stands that are relatively homogeneous at that scale. In tundra environments north of the tree line, objects such as shrubs are small relative to the MMU and their distribution tends to be governed by microclimate and microtopography, generally leading to mixed pixels.

Tundra land cover classes in many legends such as the Circumpolar Arctic Vegetation Map (CAVM) legend (Walker et al., 2002) and the modified Federal Geographic Data Committee National Vegetation Classification System (FGDC-NVCS) legend (Cihlar et al., 2003) contain many classes that are composed of several vegetation types mixed with bare soil or rock, and are described by the relative fraction each occupies in descending order. These legends do not provide quantitative fraction thresholds in the label descriptions to differentiate among classes. Rather, they are intended to be used in a more

* Corresponding author. Applications Division, Canada Centre for Remote Sensing, 588 Booth Street, Ottawa, ON, Canada K1A 0Y7. Tel.: +1 613 947 1233; fax: +1 613 947 1383.
E-mail address: iolthof@ccrs.nrca.gc.ca (I. Olthof).

0034-4257/$ - see front matter © 2006 Elsevier Inc. All rights reserved.
doi:10.1016/j.rse.2006.10.009

qualitative manner, which is in contrast to forest land cover classes that are often based on quantitative descriptions of percent tree type and cover. Describing the percentage occurrence of relatively pure land cover fractions that comprise pixels provides a quantitative land cover description. Mapping land cover fractions has the added benefit of allowing subtle spatial or temporal changes to be detected, and facilitates scaling land cover information to coarser resolutions through summation of finer scale fractions within the coarse scale pixel. Hard classifiers present difficulties doing this when several fine scale land cover types combine to produce a different land cover class within the coarse resolution pixel. For example, deciduous and coniferous fine scale forest pixels combine to produce a mixed forest pixel at a coarser resolution.

Physical linear mixture modeling is based on the energy conservation law in physics, which proposes that pixels can be represented by the linear combination of areal fractions of pure endmember signatures within the pixel instantaneous field of view (IFOV) (Drake et al., 1999). Pure reference spectral signatures are referred to as endmembers (EM) because they represent the case where 100% of the sensor's field of view is occupied by a single cover type (Lillesand & Kiefer, 2000). Strictly speaking, EMs are located at the extreme ends of a multidimensional scatter plot, but when determined in this manner, they sometimes do not represent a single meaningful cover type. In the current study, EMs are selected based on the definition by Lillesand and Kiefer (2000) as single, meaningful land cover types.

Spectral unmixing has frequently been performed to estimate a small number of sub-pixel EM fractions from Landsat imagery. The number and type of fractions are often determined based on limitations related to both unmixing method and inherent dimensionality of the spectral data. These constraints sometimes do not allow unmixing of the number or type of EMs required to model biophysical attributes on a landscape. In the current study, we make a distinction between spectral unmixing as the use of spectral endmembers input into a physical mixture model, as opposed to fractional mapping, whereby fractions may be derived through a number of modeling methods.

Numerous studies have applied linear spectral unmixing to characterize land cover as a mixture of a few, simple EM types related to the dimensionality of Landsat data. Kauth and Thomas (1976) estimated the dimensionality of Landsat multispectral imagery in developing the Kauth–Thomas Tasseled Cap transformation to derive wetness, brightness and greenness indices. In an analysis of Landsat ETM+ mixing space across a broad range of spectrally diverse land cover types using Principal Components Analysis (PCA), Small (2004) showed that more than 98% of the variance contained in the 6 reflectance channels of Landsat can be represented by the first three principal components explaining the variance in substrate, vegetation and dark surface EMs, but that all six components may contain spatially coherent information. Unmixing studies using Landsat imagery have also converged on a similar number and set of EMs related to the dimensionality of the data and methods used to unmix. Radeloff et al. (1999) applied linear unmixing to detect budworm defoliation using a three EM model consisting of shade, nonphotosynthethic vegetation and green vegetation. Ridd (1995) produced a linear unmixing model consisting of vegetation, impervious surface, and soil, which was later modified by Wu and Murray (2005) by including low and high albedo surfaces to account for variability of the impervious EM. The 3–4 general EMs normally unmixed from Landsat are limiting when attempting to characterize and map biophysical parameters across a landscape. An accurate biophysical description requires the vegetation EM to be broken down further into vegetation type.

Most image unmixing applications in the literature assume stable EM representation for all parts of the image. This assumption is not easily met, as EMs can vary from pixel to pixel within a scene (Song, 2005) or between scenes due to poor inter-scene calibration. Methods have been developed to deal with EM variability on a per-pixel basis, including the Multiple Endmember Spectral Mixture Analysis (MESMA) and the Carnegie Landsat Analysis System (CLAS). Both methods are similar in that they generate a large number of linear unmixing models using candidate EM signatures from field and image data, and select among them on a per-pixel basis to meet certain predefined error criteria. MESMA was developed in Roberts et al. (1998) and has been applied to map chaparral communities in Southern California to manage fire hazard. CLAS is an entire processing system that includes automatic atmospheric correction and spectral unmixing and has been used to map selective logging in the Amazon (Asner et al., 2005).

In an examination of EM variability in an urban environment, Song (2005) determined that mean EM signatures from the sampled distribution produce best vegetation unmixing results. In another study examining the effects of EM variability in predicting land cover from coarse (1 km) resolution data, Kerdiles and Grondona (1995) took NOAA-AVHRR land cover signatures from each of four windows and applied them using linear unmixing to the remaining three. They determined that the accuracy of fraction estimation decreased when signatures extracted from one window were applied to estimate fractions in another. Averaged land cover signatures from all four windows were found to improve overall fraction estimates. Thus, EM bias between regions implies that a local calibration is needed to achieve good local unmixing results. However, application of a locally calibrated unmixing model also requires knowledge of the area over which EMs are representative. In the absence of such information, global calibration using EM means sampled from all locations can produce acceptable global unmixing results.

A study by Fernandes et al. (2004) also considered the application of local EM signatures to unmix distant fractions. They compared 1 km fractional land cover and continuous field vegetation characteristic estimates from four different algorithms and validated using both proximate (<100 km) and distant (>400 km) Landsat land cover datasets. The four algorithms they compared included linear least-squares inversion (LLSI), a look-up table approach, artificial neural network, and linear regression calibration. Fractional land cover estimation was similar for the four methods for the proximate validation dataset, producing average root mean square errors (RMSE) in the range of 10–15% of Landsat land cover fractions. However, the distant treatment produced average RMSEs of 19–

25%, with LLSI producing the best results. The authors recommend combining multiple regression for proximate fraction estimation and LLSI for distant for optimal global unmixing results. While this study does not deal with EM variability explicitly, it nonetheless illustrates the spatial dependence of EM signatures and provides a comparative error analysis of different methods to deal with the spatial dependence problem. Olthof et al. (2005a) later showed that spectral signature spatial dependence is directional in Northern Canada, with more consistent land cover signature extension occurring in the east–west direction than in north–south due in part to different vegetation characteristics being assigned the same land cover label along the latitudinal gradient.

Numerous studies have evaluated other fractional mapping approaches from coarse resolution data, including regression trees (Defries et al., 1997; Sa et al., 2003), and a posteriori probabilities from fuzzy classifiers such as maximum likelihood, fuzzy c-means and neural networks (Bastin, 1997; Foody, 1996). Fewer studies have evaluated unmixing methods using medium resolution data from sensors such as Landsat, and even fewer studies have examined the stability of Landsat unmixing results through space or time. One study by Elmore et al. (2000) quantified the accuracy of mapped semiarid vegetation cover at 33 sites over a 14-year time-span. Using linear spectral unmixing of vegetation, soil and shade EMs, they determined their vegetation cover estimates to be within 4% of field estimates with an average bias of 2.3%. While these results are excellent, their stability was enhanced by the fact that they were monitoring the same sites through time, thereby facilitating inter-scene normalization by using identical invariant targets. An evaluation of Landsat unmixing methods and their stability through space beyond a single scene has not been performed, to the authors' knowledge, due in part to the difficulties of inter-scene radiometric normalization.

The objective of this study is to evaluate LLSI as the standard physically based linear unmixing method against other fractional mapping approaches (linear regression and regression trees) for application to a large-area normalized 90 m Landsat mosaic over northern Canada (Olthof et al., 2005c; Fig. 1). We first characterize the magnitude of the Landsat-scale mixing problem in northern environments by summarizing land cover fractions within Landsat pixels. Land cover fractions are then modeled and evaluated at three locations along an 1100 km north–south transect spanning the tree-line from forested regions of Canada to the high arctic. Finally, we apply the best models to the northern mosaic and evaluate fraction patterns and trends against independent published information on northern vegetation. While the outcome of this paper does not include biophysical modeling, future work will include the use of vegetation fractions to model a number of northern biophysical attributes, including biomass and Leaf Area Index (LAI) in order to estimate northern carbon stocks and dynamics. Eventually, we may also be able to use optimal fractional mapping methods to discern a possible climate-induced migration of the tree-line or increased shrub cover when applied to long-term data time-series (Stow et al., 2004).

Three methods are tested and compared using Landsat, Ikonos, and field data over three separate sites. All three modeling methods tested use a minimum squared error criterion implemented using traditional linear regression, regression trees (RT) and LLSI. The comparison is performed using local model calibration to predict both local and distant fractions along a north–south transect. The term 'local' is used here to refer to fractions situated at the same geographic location as calibration

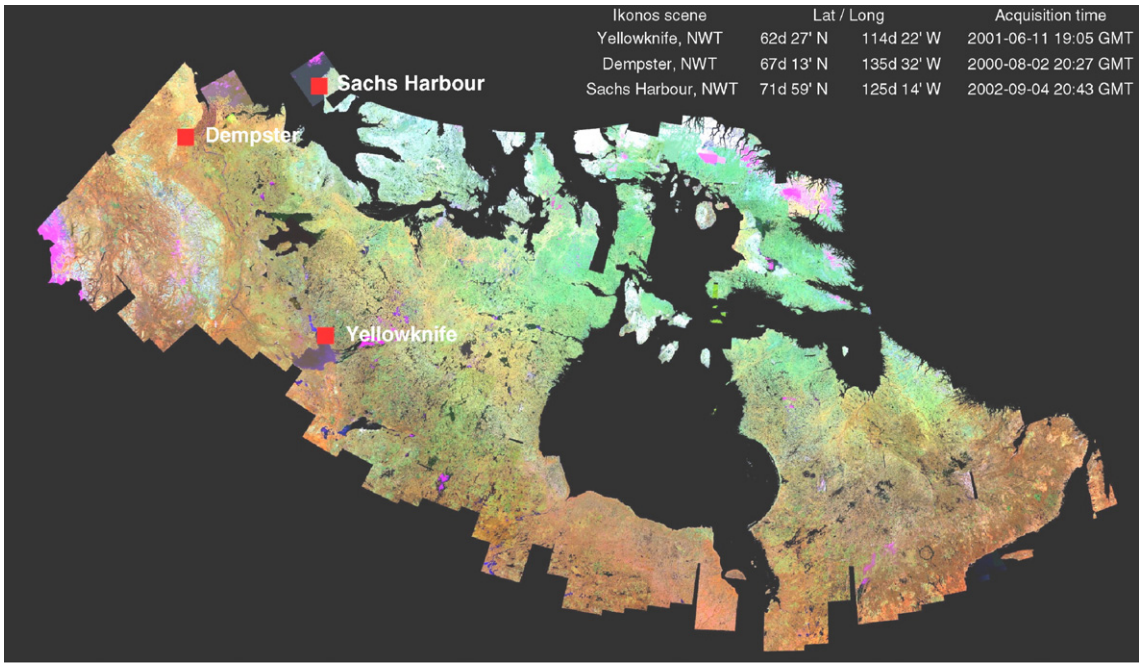

Fig. 1. Location of Ikonos scenes used to calibrate and validate unmixing models, overlain upon the Circa-2000 Landsat ETM+ mosaic of Northern Canada (Olthof et al., 2005b). Bitmaps do not represent the actual extent of Ikonos images.

data, while 'distant' refers to fractions at all locations other than the calibration site.

The five fractions selected relate to vegetation types sampled for biomass during field campaigns in the north as well as non-vegetated cover. These include 1) bare rock or soil, 2) deciduous shrub consisting of Alder, Willow, or Dwarf Birch, 3) sedges and grasses, 4) conifer, and 5) water. The shrub fraction may also include deciduous trees such as White Birch and Balsam Poplar, though these are relatively rare above the tree line.

2. Satellite sensor data and processing

2.1. Ikonos

Level 2 Ikonos data were purchased by the Geomatics for Northern Development Program of Natural Resources Canada's Earth Science Sector. Three images for which field data were available were acquired as a fine resolution data source to calibrate and validate the mixture models. These three images represent a transect south to north from below the tree line to high arctic tundra. The southernmost image is of Yellowknife, Northwest Territories (NWT), acquired June 11, 2001 and located along the northern shore of Great Slave Lake. It includes the city of Yellowknife and surrounding area consisting of Jack Pine and Black Spruce stands, Alder thickets, Dwarf Willow, sedges and grasses, rock outcrops, bare soil, and water bodies. The imagery consists of four pan-sharpened spectral bands in the visible (blue: 445–516 nm, green: 506–595 nm, red: 632–698 nm) and NIR (757–853 nm) range at 1 m spatial resolution. The second image was acquired August 2, 2000 along the Dempster Highway, NWT and contains similar land cover types as the Yellowknife scene, with fewer isolated conifer stands and shrubs, few rock outcrops, and more sedge and grass. This image was available at 4 m resolution and the same four spectral bands as the Yellowknife scene. A third image was obtained of the community of Sachs Harbour on Banks Island, NWT. It includes only bare soil and unconsolidated rock, sedge/grass and water bodies. This image was acquired at 4 m resolution and four spectral bands on September 4, 2002.

Standard Level 2 geometric correction was applied to all images, involving the use of a camera model without ground control and no orthorectification. Accuracy of Level 2 Geo products is specified at 50 m exclusive of terrain displacement. However, independent verification of Level 2 horizontal accuracy using ground control points was determined to be less than 6.5 m at the 90th percentile (Grodecki & Dial, 2001). All three scenes were of areas of moderate relief with small undulating hills, thereby producing some relief displacement in Ikonos images. Visually, Ikonos and Landsat data aligned extremely well.

The three images were classified independently to generate images of bare, shrub, grass, conifer and water. Classification was performed using fuzzy k-means to produce 150 clusters and a pseudo colour table was generated for the cluster images from each false colour NIR composite. Clusters were merged manually to the five land cover classes based on spectral and spatial proximity criteria using the Classification by Progressive Generalization (CPG) approach (Cihlar et al., 1998), where the objective is to generalize with minimal loss of information present in the original image. Cluster labeling was guided by the use of geolocated field photos acquired during two separate field campaigns along the Dempster Highway from July 17–31, 2004 and around Yellowknife July 19–28, 2005. Parks Canada field technicians working in the community of Sachs Harbour identified all major land cover types in the Sachs image with pictures and vegetation descriptions acquired in the first week of August, 2005. Once classifications were finalized, Ikonos land cover types were summed within each Landsat pixel to generate calibration and validation fractional images.

Biases may be present in the 1–4 m Ikonos classifications due to the variable response of certain land cover types and differences in solar and viewing geometry between Landsat and Ikonos. For example, the conifer cover type included sunlit conifer and adjacent deep shadow cast by conifer. These pixels may have been appropriately labeled as conifer in the interior of dense stands where shadow leads to mutual shading of trees. However, in sparse conifer or along forest edges, some shadow pixels may have been incorrectly labeled as conifer. This could have overestimated the amount of conifer present and also shrub to some degree, while underestimating grass and bare land cover types. While these biases may have existed, they are present in both the calibration and validation procedures and therefore should not have a significant bearing on our results. For example, conifer stands include shadow at 30 m resolution and therefore shadow is part of the conifer signature at this scale. Potential disparities can exist where the conifer land cover includes shadow in Ikonos but not in Landsat due to the differences in solar and viewing geometry.

2.2. Landsat

Landsat data consisted of three scenes from a seamless circa 2000 (years 1999–2002) northern Landsat band 3, 4, and 5 mosaic of Canada (Fig. 1) produced at the Canada Centre for Remote Sensing (Olthof et al., 2005c). Seventy five percent of the 446 scenes in the Landsat mosaic were acquired during the peak of growing season period in the months of July and August, including two Landsat scenes covering the areas imaged by Ikonos, while the third scene covering Sachs Harbour was acquired on September 2, 2000. All three scenes were obtained from the Centre for Topographic Information (CTI) Landsat orthoimage dataset, having a horizontal positional accuracy of 50 m or better in the north at a 90% confidence level (CTI, 2003). Landsat bands 3, 4 and 5 of the 90 m northern mosaic were radiometrically normalized to 1 km SPOT VGT apparent reflectance following the normalization method in Olthof et al. (2005b), while bands 2 and 7 for the three individual scenes were normalized to 500 m MODIS, 32-day MOD09A1 surface reflectance composite channels 4 (545–565 nm) and 7 (2105–2155 nm) from the University of Maryland's Global Land Cover Facility for the period from July 12 to August 12, 2001. The blue band (band 1) was discarded due to the effects of Rayleigh scattering on shorter wavelengths and thus the difficulties in obtaining a clear blue band for the 446 Landsat scenes in the mosaic.

The normalization method uses coarse resolution imagery with similar spectral bands to Landsat as a radiometric reference for normalizing Landsat data. Landsat data are resampled to 1 km spatial resolution to simulate the coarse resolution reference data by using a Gaussian point spread function that describes the area on earth measured by the coarse resolution sensor. Resampled Landsat pixels are then randomly sampled with spatially coincident coarse resolution pixels for each spectral band, and then regressed against the reference data using a robust regression technique called Thiel–Sen (Kendall & Stuart, 1967) to generate band and scene specific normalization coefficients. This technique and has been shown to produce similar radiometric consistency as overlap normalization methods without the need to bridge distant scenes with Landsat, or the potential for error propagation from one overlap area to the next between scenes (Olthof et al., 2005b). Data covering the area imaged by each of the three Ikonos scenes were unmixed separately at the original 30 m resolution of Landsat, and also at the resampled 90 m resolution of the northern mosaic using the same scenes and normalization coefficients at both resolutions.

3. Methods

There are two general methods used to obtain sub-pixel land cover fractions. The first involves a physically based mixture model that requires sampling EM signatures using a handheld radiometer (Adams et al., 1995), or preferably directly from the imagery thereby avoiding differences due to scale and inter-sensor calibration. The second requires statistical calibration to a range of fractional mixes, often times derived from a finer-scale classification. This method is generally more robust than the first because it includes a larger sample in the calibration procedure and is therefore less prone to sampling error (Settle & Campbell, 1998). Because both the range of fractional mixes and corresponding reflectances required for calibration are measured with error, an error minimization method such as least squares is required.

3.1. Linear least squares inversion (LLSI)

Constrained linear least squares inversion is a physically based linear unmixing method and perhaps the most common method used. LLSI uses endmember signatures to derive fractions on a per pixel basis by minimizing the squared error between the sum of the products of fractions and their EM signatures, and observed multispectral reflectance in a set of simultaneous equations. Inverting the matrices to solve the set of simultaneous equations requires the same number of equations as unknown fractions, therefore the dimensionality or number of spectral bands of the image data dictates the number of endmembers that can be unmixed. In solving for five EM fractions, Eq. (1) needs to be expanded to a set of at least five equations where λ represents discrete Landsat spectral bands.

$$R(\lambda) = f_{\mathrm{B}}\mathrm{EM}_{\mathrm{B}}(\lambda) + f_{\mathrm{S}}\mathrm{EM}_{\mathrm{S}}(\lambda) + f_{\mathrm{G}}\mathrm{EM}_{\mathrm{G}}(\lambda) + f_{\mathrm{C}}\mathrm{EM}_{\mathrm{C}}(\lambda) + f_{\mathrm{W}}\mathrm{EM}_{\mathrm{W}}(\lambda) + e(\lambda) \quad (1)$$

$$1 = f_B + f_S + f_G + f_C + f_W \quad (2)$$

Where $R(\lambda)$ is the observed reflectance in band λ, EM(λ) represents an EM signature in band λ and f represents the fraction for EMs B = bare, S = shrub G = grass, C = conifer and W = water. An additional constraint requiring fractions to sum to one is included in the set of simultaneous equations (Eq. (2)). The error term $e(\lambda)$ is minimized using singular value decomposition (Boardman, 1989; Gong et al., 1991) in the current application to unmix five EM fractions. Local spectral EM signatures at each of the three sites in five spectral bands were obtained from Landsat where the Ikonos classification represented homogeneous land cover EMs at 30 m spatial resolution, while global EMs represented a weighted average of local EMs.

3.2. Multiple linear regression

Multiple regression also uses least squares error minimization, but predicts each fraction B, S, G, C, W from the multispectral data independently (Iverson et al., 1994) and therefore fractions may not sum to one. However, fractions may be constrained a posteriori to sum to one by calculating fraction percentage occurrence on a per pixel basis. To predict fractions using three spectral bands, calibration involves deriving coefficients a, b and c that minimize the error e between observed multispectral reflectance r from bands i, j and k and fractions f from a calibration dataset (Eq. (3)).

$$\begin{aligned} f_{\mathrm{B}} &= a_{\mathrm{B}}r_i + b_{\mathrm{B}}r_j + c_{\mathrm{B}}r_k + e_{\mathrm{B}} \\ f_{\mathrm{S}} &= a_{\mathrm{S}}r_i + b_{\mathrm{S}}r_j + c_{\mathrm{S}}r_k + e_{\mathrm{S}} \\ f_{\mathrm{G}} &= a_{\mathrm{G}}r_i + b_{\mathrm{G}}r_j + c_{\mathrm{G}}r_k + e_{\mathrm{G}} \\ f_{\mathrm{C}} &= a_{\mathrm{C}}r_i + b_{\mathrm{C}}r_j + c_{\mathrm{C}}r_k + e_{\mathrm{C}} \\ f_{\mathrm{W}} &= a_{\mathrm{W}}r_i + b_{\mathrm{W}}r_j + c_{\mathrm{W}}r_k + e_{\mathrm{W}} \end{aligned} \quad (3)$$

Because multiple regression does not solve a set of simultaneous equations, the number of fractions is not constrained by the number of dimensions available in the dataset. In a comparison of LLSI and multiple regression, Settle and Campbell (1998) showed that the difference between the two estimators is less than the prediction error when mixing is linear and signatures are well separated. This implies that multiple regression can be an acceptable alternative to LLSI for spectral unmixing when these conditions are met.

3.3. Regression trees

Regression trees are used to predict a continuous dependent variable from one or more continuous and/or categorical independent variables. They offer certain advantages over other classification methods in that they are non-parametric and make no assumptions about the form (linear or non-linear) or the nature (monotonic or nonmonotonic) of the relationship between predictor and dependent variables. They are also simple to interpret and easily implemented as a series of if-then statements applied to the independent variables to determine a set of end-nodes representing discrete, homogeneous distributions of the dependent variable (Defries et al., 2000) (Fig. 2).

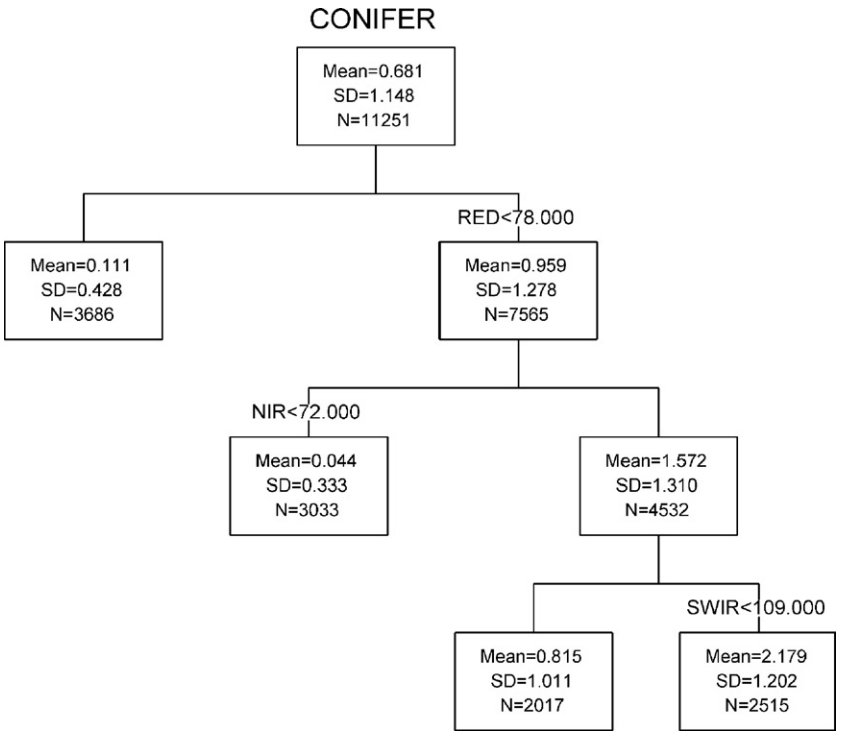

Fig. 2. Globally calibrated regression tree used to predict the conifer fraction from 3 spectral bands available in the 90 m northern Landsat mosaic.

Node splitting is performed to generate the best prediction by recursively minimizing the impurity or heterogeneity of nodes relative to parent nodes. Heterogeneity is measured as the sum of squares between dependent observations and node means (Eq. (4)).

$$\mathrm{SS}(t) = \frac{1}{N(t)} \sum_{i=1} n_i (f_i - \bar{f}(t))^2 \quad (4)$$

Where $N(t)$ is the number of cases in node t, n_i is the value of the frequency variable, f_i is the value of the response variable (fraction i) and $\bar{f}(t)$is the mean fraction for node t. Parent node splitting continues until one of the following specified criteria are met: a maximum number of 23 splits, a minimum of 5% reduction in error, or a minimum of five cases in each node. For all regression tree models, fractions were binned into 20% intervals, producing parent nodes that were sufficiently heterogeneous to allow node splitting based on the specified error reduction criterion. Individual fractions predicted separately were constrained to sum to one on a pixel basis.

3.4. Experimental design and validation

Comparisons of prediction errors were made to evaluate four factors that affect fractional mapping results. These included: 1) fractional mapping method among LLSI unmixing, regression and regression tree modeling; 2) local calibration of an individual scene vs. global calibration using all three scenes; 3) local and distant land cover fraction prediction; and 4) spatial resolution of 30 m and 90 m to determine the information loss caused by resampling to a coarser resolution. Sachs Harbour calibration was performed to predict local fractions only, due to the fact that only three of the five land cover types were present in the Sachs scene while all five were present in the other two. However, both the Dempster and Yellowknife models were applied to Sachs Harbour to evaluate the commission errors predicting the two fractions that were not present. Error measures used in these assessments included the Root Mean Square Error (RMSE) between fractions from Ikonos and those predicted by Landsat, the correlation coefficient to determine spatial agreement between the two, and average absolute bias among scene fractions. Note that, although no formal validation was conducted for the Ikonos maps that were used to generate the "ground truth" fractions, they were carefully developed and labeled using field vegetation surveys. Regardless of their true accuracy, they provide a reasonable benchmark in this study for comparing results from the different Landsat fractional modeling methods.

The ultimate goal is to map land cover fractions in the 90 m northern Landsat mosaic for biophysical modeling. Because these data are currently available in three spectral bands only, we first perform a local validation to assess prediction error differences over each calibration scene for all three methods (LLSI, regression and regression trees) and both three (ETM+ bands 3–5) and five (ETM+ bands 2–5 and 7) spectral band sets. Of the methods that predict calibration data best, we then evaluate the potential to extend locally calibrated models to map distant land cover fractions at other Ikonos scene locations. We also evaluate models calibrated using data from all three scenes – referred to as global calibrations – to map fractions at all three scenes. The previous analyses are performed by calibrating and validating at the original 30 m resolution of Landsat. We then evaluate the

application of the above models to map fractions from resampled 90 m Landsat and three spectral bands available in the northern Landsat mosaic. Lastly, we combine models that predict each fraction best and report errors over the three sites.

4. Results

An examination of Landsat-scale mixing at both 30 m and 90 m resolutions for the three calibration sites revealed differences in heterogeneity due to both scale and site (Fig. 3). The dominant fraction occupied between ~67 and 87% of 30 m pixels and between ~62 and 84% of 90 m pixels from south to north, while the cumulative fraction of the three most dominant varied between ~95–100% and ~91–100% at 30 m and 90 m, respectively. The three fractions present at Sachs Harbour (bare, grass and water) represented three dominant fractions, while dominant fractions varied from pixel to pixel at the other two sites. Heterogeneity differences among sites may be more pronounced than what is shown in Fig. 3, since the average dominant fraction at Yellowknife included a large number of pure water pixels.

EMs sampled directly from 30 m Landsat pixels where the EM fraction was 100% are plotted for the three calibration sites in Fig. 4. There were no pure conifer pixels at Yellowknife and no conifer or shrub exist at Sachs Harbour. Error bars representing 1 standard deviation on signatures show potential for spectral confusion between grass and shrub EMs at the Dempster site, while too few pure shrub pixels occurred at Yellowknife to draw the same conclusion. Of the EM signatures represented by a reasonably large number of pixels, the bare signatures were most varied at all three sites.

4.1. Local validation

Linear regression with five spectral bands produced slightly better RMSE, correlation and bias than regression trees with five bands, followed by regression and regression trees with three bands (Table 1). LLSI produced larger errors than other methods for Yellowknife and Dempster and errors comparable to other methods for Sachs Harbour. LLSI requires the same number of spectral bands as fractions for unmixing, however, results

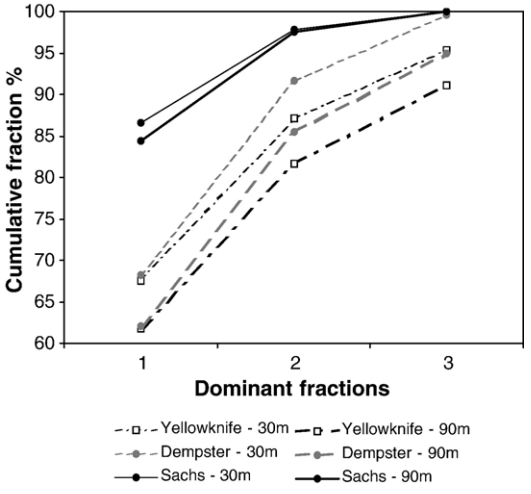

Fig. 3. Cumulative sum of the dominant fraction (1) occupying the greatest proportion of a Landsat pixel, and sub-dominant fractions (2, 3) occupying progressively lower Landsat pixel proportions for the three calibration sites and two spatial resolutions.

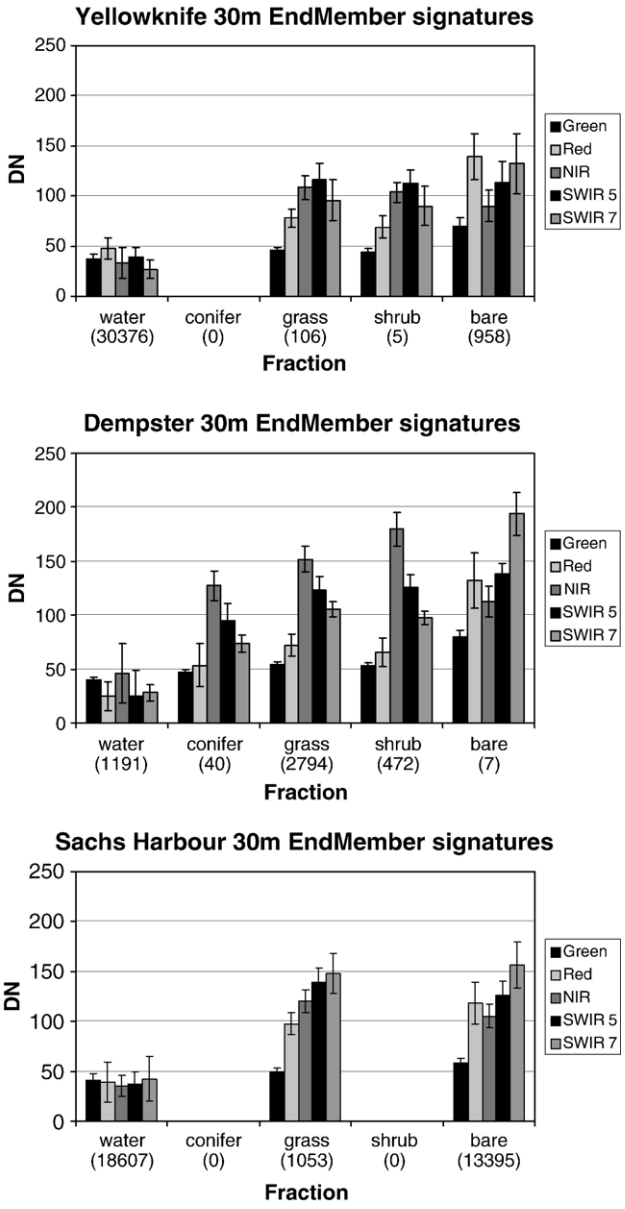

Fig. 4. Pure endmembers sampled from 30 m Landsat DNs normalized across the three calibration sites. The number of Landsat pixels included in each sample is shown in brackets.

Table 1
Local validation results, N=316,044 30 m pixels

Method	# ETM+ bands	RMSE	R^2	Absolute bias
Regression	3	16.34	0.66	3.12
RT	3	15.50	0.65	3.62
LLSI	5	24.27	0.40	7.12
Regression	5	**14.53**	**0.72**	**0.92**
RT	5	14.66	0.71	2.03

The lowest errors among methods are in bold.

depend more on the inherent dimensionality of the spectral bands input into LLSI than the absolute number of bands. Small (2004) and others have estimated the dimensionally of Landsat at three, and a principal components analysis of the three Landsat scenes and five spectral bands in the current study produced a similar conclusion, with the three low order PCs accounting for more than 96% of the variance contained in the full five band set. Factor loadings on the three primary PCs were also similar to those determined by Small (2004). Therefore, unmixing five fractions with five spectral bands is effectively underdetermined because of redundant information contained in multiple spectral bands, while unmixing three fractions at Sachs Harbour was sufficiently determined due to the dimensionality of the data, and therefore produced good results.

Another possible explanation for the relatively poor overall performance of LLSI is that this method, unlike other methods tested here, is not trained using the data population, which has the effect of a priori weighting these classifiers to the more populous EM combinations. Because LLSI was unable to predict calibration data as accurately as other methods, no attempt was made at extending LLSI models to unmix distant land cover fractions.

4.2. Model extension — distant validation

Model extension results for predicting distant land cover fractions are shown in Table 2. Model extension was performed using Yellowknife and Dempster models only to predict fractions at distant sites, while Sachs models were not extended due to incomplete representation of fractions present at other sites. Overall, regression using three spectral bands produced the best results, with predicted fractions having the highest correlation and lowest bias compared to mapped fractions from Ikonos. While the regression tree model with five bands produced the lowest RMSE with observed fractions, all models produced RMS errors that were within 1.3%, and biases within 1.7% of each other. The similar performance of three band models compared to five band models suggests that the additional two spectral bands provide very little extra information related to the selected land cover fractions. While five band models produced superior results for predicting local fractions, their similar or inferior ability to predict distant fractions suggests overfitting to calibration data at the expense of robustness for model extension.

4.3. Global calibration and validation

Global calibration models trained using data from all three scenes (Table 3), show superior results for the three band regression tree in terms of RMSE and bias, followed by the other methods depending on which criterion is used for evaluation. These results reflect the ability of methods to simultaneously predict local and distant land cover fractions using calibration data from all three scenes.

Specifically, results reveal both the robustness of methods to sub-optimal calibration for local fraction prediction, while at the same time out-performing locally calibrated models for distant fraction prediction. They also reveal robustness against overfitting to data from one area by their consistency in predicting each area separately. The absolute bias averaged over five fractions was lowest and most consistent over the three sites for the three band regression tree compared to other methods. An examination of the coefficients for all global regression models (Table 4) shows similar loadings on spectral bands between three and five band models, with highest loadings for all five band models occurring on bands 3, 4 and 5 included in the northern mosaic. The greatest differences in spectral loadings exist for the water models, as water is predicted primarily from SWIR band 5 from the three band set, while it is predicted mainly from NIR band 4 and SWIR band 7 from the five band set. Due to the similar performance between three and five band models, the minimal contribution of bands 2 and 7 for predicting fractions and the objective of determining land cover fractions from the 90 m, three band northern Landsat mosaic, five band models will not be considered further.

4.4. Fraction estimation from resampled 90 m Landsat data

Fractions were estimated from 90 m data by applying global models calibrated using 30 m data and three spectral bands to

Table 2
Model extension (local calibration/distant validation) results, N=406,603 30 m pixels

Method	# ETM+ bands	RMSE	R^2	Absolute bias
Regression	3	24.78	**0.60**	**11.41**
RT	3	24.53	0.49	13.10
Regression	5	25.14	0.59	13.06
RT	5	**23.84**	0.54	12.27

The lowest errors among methods are in bold.

Table 3
Global calibration results, N=316,044 30 m pixels

Method	# ETM+ bands	RMSE	R^2	Absolute bias
Regression	3	17.95	**0.63**	4.66
RT	3	**17.13**	0.61	**2.63**
Regression	5	17.38	**0.63**	3.68
RT	5	17.61	0.60	3.87

The lowest errors among methods are in bold.

Table 4
Linear regression coefficients for 3 and 5 band models, N=316,044 30 m pixels

	Green	Red	NIR	SWIR5	SWIR7
3 band regression model coefficients					
Bare		**0.785**	−0.377	0.274	
Shrub		−0.163	**0.463**	−0.205	
Grass		−0.432	−0.057	**0.709**	
Conifer		−0.236	**0.309**	−0.182	
Water		0.000	−0.331	**−0.563**	
5 band regression model coefficients					
Bare	0.067	**0.544**	−0.23	−0.293	0.517
Shrub	−0.033	−0.102	**0.481**	−0.17	−0.076
Grass	0.23	−0.431	−0.087	**0.782**	−0.059
Conifer	−1.682	0.117	**0.404**	−0.294	0.056
Water	1.691	−0.179	**−0.589**	0.05	−0.493

The highest loadings on each fraction are in bold.

Table 5
30 m global calibration/90 m application and validation N=35,393 90 m pixels

Method	# ETM+ bands	RMSE	R^2	Absolute bias
Regression	3	16.86	**0.62**	4.86
RT	3	**16.81**	0.58	**2.69**

The lowest errors among methods are in bold.

approximate errors in predicting fractions from the northern Landsat mosaic over the three scenes (Table 5). Errors were similar between the two spatial resolutions, with RMSE improving by <1% at 90 m resolution and correlation and bias becoming slightly worse compared to 30 m fraction estimation. These results suggest that globally calibrated 30 m models with three spectral bands can by applied to predict fractions from 90 m data with only a minimal loss of information.

In tracking errors through the preceding set of experiments, it can be seen that methods that used five spectral bands predicted calibration data better than three band models, but tended to overfit to calibration data as model extension was worse for five band models. Global calibration produced intermediate results between local and distant validation, with three band models performing similar to, or even out-performing five band models. This suggests that three bands may be sufficient to accurately estimate these land cover fractions and that additional two bands provide little unique information. Given that three bands models may be considered appropriate to predict fractions at 30 m resolution, they may also be considered sufficient at 90 m resolution since there was a minimal loss of information in the application of 30 m models to resampled 90 m data.

4.5. Model combination for northern land cover fraction estimation

Overall fraction prediction was best for globally calibrated regression trees at both 30 m and 90 m resolutions, with an average RMSE for the three scenes of less than 17%, an average correlation coefficient of 0.55 and an absolute bias of less than 3%. Maximum bias was between −6% and +6%, representing different cover types in the three scenes. An examination of individual fractions predicted by this method revealed acceptable results for all fractions, except that the spatial distribution of the shrub fraction measured using correlation was not well predicted with the RT, perhaps due to spectral confusion between shrub and grass, although the shrub bias was acceptably low. Another likely explanation for lower correlations stemming from RT models compared to regression is that RT predicts fractional classes binned into 20% intervals, while regression predicts continuous fractions. While the variance within each RT fractional map is enhanced when constraining fractions to sum to one by including some of the variance in other fractions, RT fractional maps nonetheless remain more generalized than regression maps, thereby leading to lower correlations against continuous fractions from Ikonos. Linear regression predicted shrub better than any other method, while RT predicted all other fractions better (Fig. 5; Table 6). Therefore, we decided to combine linear regression for shrub, and RT to predict other fractions individually, and then constrain fractions to sum to one.

Table 6
90 m regression tree and linear regression errors by fraction, N=35,393 90 m pixels

	Regression trees			Linear regression		
	R^2	RMSE	Absolute bias	R^2	RMSE	Absolute bias
Bare	**0.56**	**16.51**	**3.51**	0.62	16.50	5.83
Shrub	0.26	12.44	4.17	**0.51**	**11.29**	**2.22**
Grass	**0.49**	**23.10**	**1.03**	0.55	21.23	4.95
Conifer	**0.66**	**14.31**	**2.57**	0.47	16.23	5.85
Water	**0.81**	**17.70**	**2.16**	0.81	19.05	5.48

The lowest errors among methods are in bold.

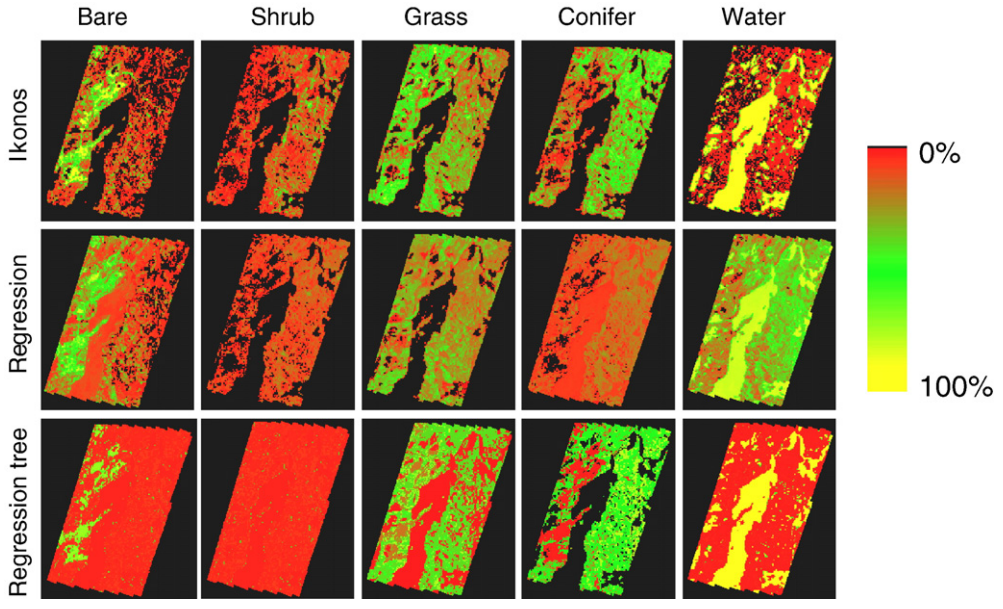

Fig. 5. Ikonos fractions and globally calibrated regression and regression tree models applied to the Yellowknife Landsat data at 90 m spatial resolution.

Table 7
90 m errors stemming from 30 m globally calibrated linear regression for the shrub endmember and regression trees for other four endmembers, N=35,393 90 m pixels

	RMSE	R^2	Absolute bias	Max bias	Class
Yellowknife	18.97	0.60	2.08	3.22	Conifer
Dempster	15.19	0.55	1.49	−2.55	Grass
Sachs	15.14	0.68	2.02	−4.22	Bare
Average	16.43	0.61	1.87		

Combining a globally calibrated linear regression model for the shrub cover type and globally calibrated regression trees for other fractions resulted in an average RMSE of 16.43%, an average correlation coefficient of 0.61, and an average absolute bias of 1.87%, which indicates better EM fraction prediction than regression trees by themselves. Maximum biases were between 3.22% and −4.22% for the Yellowknife conifer, and Sachs bare fractions, respectively (Table 7). Therefore, in the south around Yellowknife, we overestimated conifer by about 3%, while in the north around Sachs Harbour, we underestimated the bare fraction by just over 4%. By comparison, the best local calibrations at each of the three sites using regression trees for Yellowknife and Sachs Harbour and linear regression for Dempster, produced an average RMSE of 15.69%, an average correlation coefficient of 0.64, and an average absolute bias of 1.82%. Therefore, if stratification were possible and assuming local calibrations were representative of their strata, errors would decrease only slightly from the global calibration using combined linear regression and regression trees to predict separate fractions.

5. Discussion

We applied regression tree and linear regression models to the northern Landsat mosaic (Fig. 6), as described in the preceding section on combining models. Visually, results appear promising, as several known vegetation features are present in this set of fractional maps. The bare fraction map clearly shows portions of Labrador and northern Quebec as well as the northern islands to be mostly barren, as well as mountain ranges in the Yukon. Further south, barren regions mix more with grass. The shrub fraction map depicts shrublands around the Mackenzie Delta, as well as a known anomaly west of Hudson Bay that includes combined shrub and tree cover in the range of 20–45%, which is higher than the surrounding tundra (Timoney, 1995). The conifer fraction map accurately delimits Canada's treeline by comparison to a map of the forest-tundra transition zone that was created using air photo interpretation and reconnaissance (Fig. 7) (Timoney et al., 1992). The water fraction map shows all major water bodies, however, there appears to be some confusion between conifer and water along the north shore of the St. Lawrence in eastern Canada.

While these results are promising, additional calibration data in the form of 1–4 m resolution satellite imagery or airphotos need to be collected to better calibrate and evaluate fractional mapping models across the whole area. As mentioned

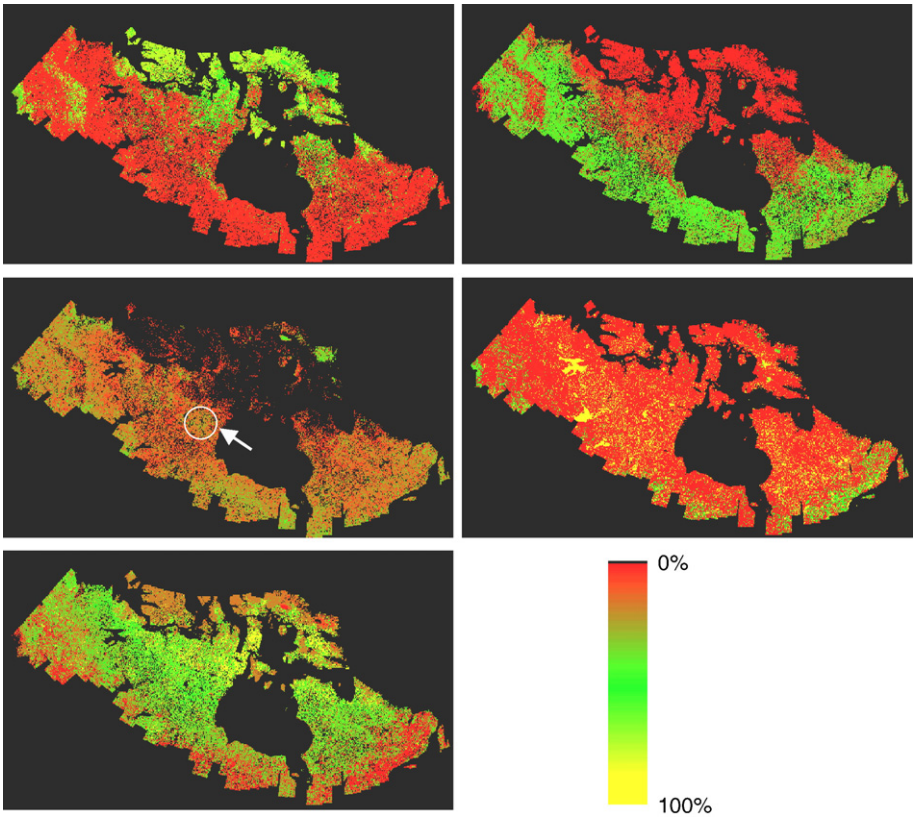

Fig. 6. Fractional maps of Northern Canada derived from regression and regression tree models applied to the 90 m Landsat ETM+ mosaic in Fig. 1. The shrub fraction map highlights a known vegetation anomaly west of Hudson Bay where combined shrub and tree cover are in the range of 25–45% (Timoney, 1995).

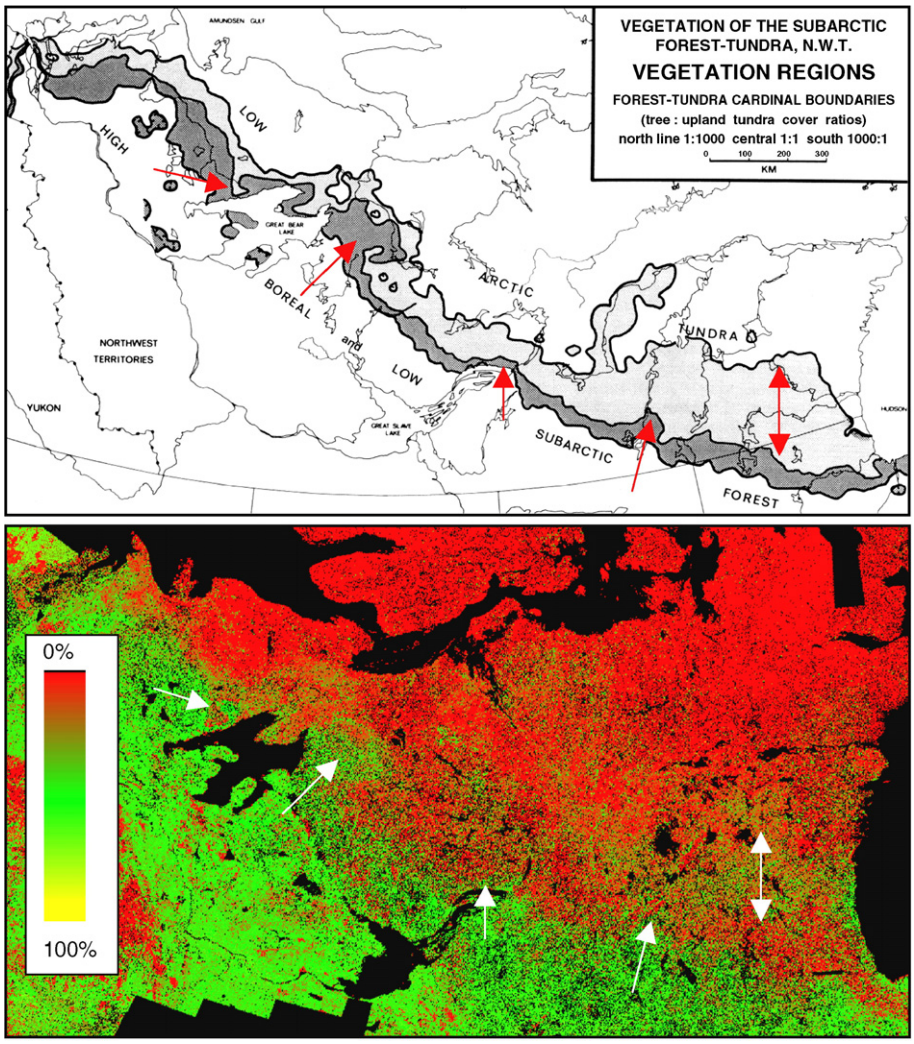

Fig. 7. Comparison of Canada's forest-tundra ecotone mapped using 1314 air photos (1:50,000) and extensive ground truthing (from Timoney et al., 1992) and the fractional conifer map derived using 90 m resample Landsat imagery. The middle line in the upper panel represents a 1:1 tree:tundra cover ratio and the dark and light shaded areas represent 1000:1 and 1:1000 ratios, respectively. The arrows show matching patterns of interest.

previously, locally calibrated models and their application to local regions require knowledge of the spatial representativeness of signatures and models to stratify to those extents. One obvious source of error caused by land cover variability is in the bare land cover type. A geological fault can be seen in the Yellowknife Ikonos scene that joins two bedrock types with very different spectral signatures. One rock unit consists of a mafic intrusion, which is dark in colour, while the other is much brighter, consisting of resistant felsic minerals such as silica and feldspar contained in undivided sedimentary rocks (Wheeler et al., 1997).

Variability in the bare signature leads to sub-optimal global fractional mapping results when assigned a single signature. Other authors have noted bare or soil EM signature variability as the most significant source of error in mixture modeling. Small (2004) noted that substrate was the most compositionally variable and least constrained EM in the Landsat mixing space. Others (e.g. Wu & Murray, 2005) have included an additional EM to the common three EM model to account for variability in the impervious, bare EM signature. Much of northern Canada is barren due to climatic constraints on plant growth; therefore, characterizing the variability in barren surfaces is important to achieve accurate fractional mapping results across the region. A geological map of Canada exists and may provide some insight into the distribution of rock types and their signatures, although preliminary analysis suggests that this map may be too generalized to accurately delineate their extent. The problem of bare signature variability is compounded by lichens that commonly grow on rock outcrops and can themselves be quite variable depending on type (Rees et al., 2004; Zhang et al., 2005).

As other authors have noted, representing a landscape with a few EMs is a gross generalization of the real world and assuming that EMs have stable signatures through space is an even greater simplification (Small, 2004; Song, 2005). Among the three locations used to calibrate models, there is spatial variation in both geology and vegetation. This is especially pronounced in the latitudinal gradient where climatic factors produce shifts in plant species assemblages. These shifts are manifested in reflectance differences controlled by plant biophysical and biochemical structure. For example, sample

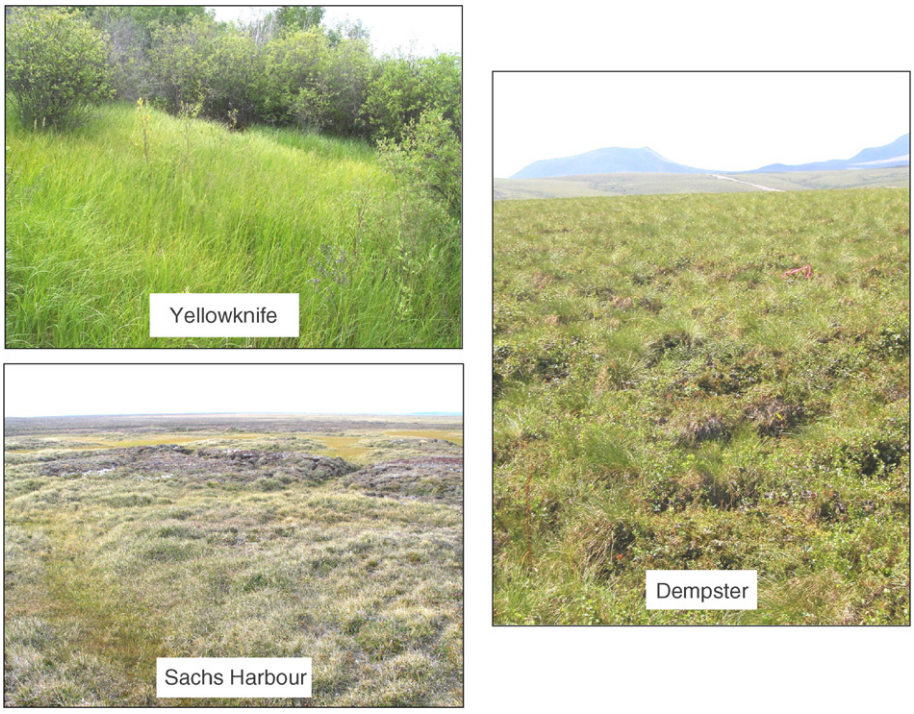

Fig. 8. Grass endmember pictures taken near peak of growing season at each of the three Ikonos scene locations show endmember variability due to greenness, senescence, hummocks, interspersed dwarf shrub and lichen.

field pictures taken near mid-summer of the grass land cover type for the three locations are shown in Fig. 8. At this time of year, grass is greenest at Yellowknife and becomes less green and more senescent further north, and also occurs more in hummocks, is more mixed with lichen and dwarf shrub, among other differences that contribute to grass signature variability. Because this study was performed along a latitudinal gradient, extending mixture models in this direction can be considered as a worst-case scenario.

EM signatures vary not only through space, but also through time. Vegetation phenology, from green-up in the spring to senescence in the fall, will affect EM signatures and is not constant from north to south. Generally, we assume that near peak of growing season image acquisitions during the months of July and August should contain relatively consistent EM signatures. However, the window corresponding to the timing of peak of growing season becomes narrower further north and therefore seasonal effects may be more pronounced. A lack of correspondence between the timing of calibration data acquisitions and data in the mosaic to which models are applied also leads to sub-optimal unmixing results. The Landsat scene containing Sachs Harbour was acquired in the beginning of September, and because of its high northern latitude, may not be representative of peak season conditions elsewhere. Some of these seasonal effects may be at least partially controlled due to Landsat scenes being radiometrically normalized to peak of growing season 1 km VGT imagery. Precipitation and unseasonable temperatures also contribute to signature variability, but in an unsystematic way. Both spatial and temporal signature variability will contribute to the errors reported in this paper.

Future work will include obtaining and classifying other high spatial resolution data in areas where we have already acquired field validation data. Other Ikonos scenes have been collected, though they either lack suitable reference data or contain too much topographic variation to be currently of use. Spatial databases such as the Geological Map of Canada and Ecological Framework for Canada will be evaluated to stratify Landsat data and others such as long-term climate data will be assessed to constrain the number and nature of land cover signatures over different parts of Canada following the approach in Pavlic et al. (in press). Alternatively, selection among candidate endmembers (e.g. bare substrate types) for each pixel could be based on minimizing the RMS error among mixture models as is proposed by multiple endmember spectral mixture analysis (MESMA) (Dennison & Robers, 2003). Temporal signature variability will be investigated by examining phenological trends in multi-temporal 10-day SPOT VGT composites of homogeneous 1 km areas identified in the 90 m Landsat data. A new generation of sensors such as MODIS and MERIS that acquire multi-temporal data at 250–300 m will be evaluated as a primary data source for fractional mapping, although MODIS may be limited by having only two spectral bands while MERIS contains 15. Finally, biophysical mapping and modeling will be conducted based on vegetation fractions obtained from these data and methods.

6. Conclusions

This paper evaluated factors influencing the accuracy of northern fractional mapping from Landsat, including spatial resolution, modeling method, and source of calibration/

validation data. Using field, Ikonos, and Landsat data (at 30 and 90 m spatial resolutions), we predicted five land cover fractions including bare, water, deciduous shrub, grass, and conifer along an 1100 km north–south transect spanning the tree-line. A physically based linear unmixing algorithm was evaluated against linear regression and regression tree modeling using local and global calibrations to predict both local and distant land cover fractions. Regression tree modeling and global calibration of individual fractions constrained a posteriori to sum to one was the best method overall at both 30 and 90 m resolutions. However, it predicted the spatial distribution of shrub poorly while bias was acceptably low. Linear regression modeling predicted the shrub fraction better than the regression tree; therefore, we combined the globally calibrated linear regression model to predict shrub with regression trees to predict the remaining four land cover fractions. This combined approach achieved a RMSE of 16.43%, a correlation coefficient of 0.61, and an average absolute bias of 1.87% against Ikonos fractions at 90 m resolution. These results are comparable to the best locally calibrated models applied to the calibration datasets, and avoids the problem of having to stratify Landsat to the area where models and land cover signatures are representative.

Acknowledgements

The authors are grateful to David Haogak and Jacquie Bastick of Aulavik National Park, Parks Canada for graciously providing site photos and vegetation descriptions around Sachs Harbour. Costas Armenakis provided satellite image data through the Geomatics for Northern Development Program of Natural Resources Canada. We thank Richard Fernandes and three anonymous reviewers for their constructive comments. Partial funding was provided by the Canadian Space Agency through the Government Related Initiatives Program.

References

Adams, J. B., Sabol, D. E., Kapos, V., Almeida Filho, R., Roberts, D. A., Smith, M. O., et al. (1995). Classification of multispectral imagery based on fractions of endmembers: Application to land-cover change in the Brazilian Amazon. *Remote Sensing of Environment*, *52*, 137–154.

Asner, G. P., Knapp, D. E., Broadbent, E. N., Oliveira, P. J. C., Keller, M., & Silva, J. N. (2005). Selective logging in the Brazilian Amazon. *Science*, *310*, 480–482.

Bastin, L. (1997). Comparison of fuzzy c-means classification, linear mixture modeling and MLC probabilities as tools for unmixing coarse pixels. *International Journal of Remote Sensing*, *18*, 3629–3648.

Boardman, J. W. (1989). Inversion of imaging spectrometry data using singular value decomposition. *Proc. of the 1989 International Geoscience and Remote Sensing Symposium (IGARSS '89) and the 12th Canadian Symposium on Remote Sensing. Vancouver, BC, Canada*, *Vol. 4* (pp. 2069-2072).

Centre for Topographic Information (CTI) (2003). *Landsat 7 orthorectified imagery over Canada, level 1 product specifications*, edition 1 Ottawa, Ont.: Natural Resources Canada Centre for Topographic Information.

Cihlar, J., Xiao, Q., Chen, J., Beaubien, J., Fung, K., & Latifovic, R. (1998). Classification by progressive generalization: A new automated methodology for remote sensing multichannel data. *International Journal of Remote Sensing*, *19*, 3141–3168.

Cihlar, J., Latifovic, R., Beaubien, J., Guindon, B., & Palmer, M. (2003). Thematic Mapper (TM) based accuracy assessment of a land cover product for Canada derived from SPOT VEGETATION (VGT) data. *Canadian Journal of Remote Sensing*, *29*, 154–170.

Defries, R., Hansen, M., Steininger, M., Dubayah, R., Sohlberg, R., & Townshend, J. (1997). Subpixel forest cover in Central Africa from multisensor, multitemporal data. *Remote Sensing of Environment*, *60*, 228–246.

Defries, R. S., Hansen, M. C., & Townshend, J. R. G. (2000). Global continuous fields of vegetation characteristics: A linear mixture model applied to multi-year 8 km AVHRR data. *International Journal of Remote Sensing*, *21*, 1389–1414.

Dennison, P. E., & Robers, D. A. (2003). Endmember selection for multiple endmember spectral mixture analysis using endmember average RMSE. *Remote Sensing of Environment*, *87*, 123–135.

Drake, N. A., Mackin, S., & Settle, J. J. (1999). Mapping vegetation, soils, and geology in semiarid shrublands using spectral matching and mixture modeling of SWIR AVIRIS imagery. *Remote Sensing of Environment*, *68*, 12–25.

Elmore, A. J., Mustard, J. F., Manning, S. J., & Lobell, D. B. (2000). Quantifying vegetation change in semiarid environments: Precision and accuracy of spectral mixture analysis and the normalized difference vegetation index. *Remote Sensing of Environment*, *73*, 87–102.

Fernandes, R., Fraser, R., Latifovic, R., Cihlar, J., Beaubien, J., & Du, Y. (2004). Approaches to fractional land cover and continuous field mapping: A comparative assessment over the BOREAS study region. *Remote Sensing of Environment*, *89*, 234–251.

Foody, G. M. (1996). Approaches for the production and evaluation of fuzzy land cover classifications from remotely-sensed data. *International Journal of Remote Sensing*, *17*, 1317–1340.

Gong, P., Miller, J., Freemantle, J., & Chen, B. (1991). Spectral decomposition of Landsat thematic mapper data for urban land-cover mapping. *Proc. of the 14th Canadian Symposium on Remote Sensing, Calgary, Alberta, Canada, May 1991*.

Grodecki, J., & Dial, G. (2001). Ikonos geometric accuracy. http://www.spaceimaging.com/whitepapers_pdfs/2001/IKONOS%20Geometric%20Accuracy-ISPRS%202001.pdf

Iverson, L. R., Cook, E. A., & Graham, R. L. (1994). Regional forest cover estimation via remote sensing: The calibration center concept. *Landscape Ecology*, *9*, 159–174.

Kauth, R. J., & Thomas, G. S. (1976). The Tasseled Cap — A graphic description of the spectral-temporal development of agricultural crops as seen by Landsat. *Proceedings of the Symposium on Machine Processing of Remotely Sensed Data* (pp. 4041–4051).

Kendall, M. G., & Stuart, A. S. (1967). *Advanced Theory of Statistics*, *Vol. 2*. London: Charles Griffin and Company.

Kerdiles, H., & Grondona, M. O. (1995). NOAA-AVHRR NDVI decomposition and subpixel classification using linear mixing in the Argentinean Pampa. *International Journal of Remote Sensing*, *16*, 1303–1325.

Lillesand, T. M., & Kiefer, R. W. (2000). *Remote sensing and image interpretation*, 4th edition New York: John Wiley & Sons, Inc.

Olthof, I., Butson, C., Fernandes, R., Fraser, R., Latifovic, R., & Orazietti, J. (2005). Landsat ETM+ mosaic of northern Canada. *Canadian Journal of Remote Sensing*, *31*, 412–419.

Olthof, I., Butson, C., & Fraser, R. (2005). Signature extension through space for northern landcover classification: A comparison of radiometric correction methods. *Remote Sensing of Environment*, *95*, 290–302.

Olthof, I., Pouliot, D., Fernandes, R., & Latifovic, R. (2005). Landsat ETM+ radiometric normalization comparison for northern mapping applications. *Remote Sensing of Environment*, *95*, 388–398.

Pavlic, G., Chen, W., Fernandes, R., Cihlar, J., Price, D. T., Latifovic, R. (in press). Canada-wide maps of dominant tree species from remotely sensed and ground data.

Radeloff, V. C., Mladenoff, D. J., & Boyce, M. S. (1999). Detecting Jack Pine budworm defoliation using spectral mixture analysis: Separating effects from determinants. *Remote Sensing of Environment*, *69*, 156–169.

Rees, W. G., Tutubalina, O. V., & Golubeva, E. I. (2004). Reflectance spectra of subarctic lichens between 400 and 2400 nm. *Remote Sensing of Environment*, *90*, 281–292.

Ridd, M. K. (1995). Exploring a V–I–S (vegetation–impervious surface–soil) model for urban ecosystem analysis through remote sensing: Comparative anatomy for cities. *International Journal of Remote Sensing*, *16*, 2165–2185.

Roberts, D. A., Gardner, M., Church, R., Ustin, S., Scheer, G., & Green, R. O. (1998). Mapping chaparral in the Santa Monica Mountains using multiple endmember spectral mixture models. *Remote Sensing of Environment*, *65*, 267−279.

Sa, A. C. L., Pereira, J. M. C., Vasconcelos, M. J. P., Silva, J. M. N., Ribeiro, N., & Awasse, A. (2003). Assessing the feasibility of sub-pixel burned area mapping in miombo woodlands of northern Mozambique using MODIS imagery. *International Journal of Remote Sensing*, *24*, 1783−1796.

Settle, J., & Campbell, N. (1998). On the errors of two estimators of subpixel fractional cover when mixing is linear. *IEEE Transactions on Geoscience and Remote Sensing*, *36*, 163−169.

Small, C. (2004). The Landsat ETM+ spectral mixing space. *Remote Sensing of Environment*, *93*, 1−17.

Song, C. (2005). Spectral mixture analysis for subpixel vegetation fractions in the urban environment: How to incorporate endmember variability? *Remote Sensing of Environment*, *95*, 248−263.

Stow, D. A., Hope, A., McGuire, D., Verbyla, D., Gamon, J., Huemmrich, F., et al. (2004). Remote sensing of vegetation and land-cover change in Arctic Tundra Ecosystems. *Remote Sensing of Environment*, *89*, 281−308.

Timoney, K. (1995). Tree and tundra cover anomalies in the subarctic forest-tundra of Northwestern Canada. *Arctic*, *48*, 13−21.

Timoney, K. P., La Roi, G. H., Zoltai, S. C., & Robinson, A. G. (1992). The high subarctic forest-tundra of Northwestern Canada: Position, width, and vegetation gradients in relation to climate. *Arctic*, *45*, 1−9.

Walker, D. A., Gould, W. A., Maier, H. A., & Raynolds, M. K. (2002). The circumpolar arctic vegetation map: AVHRR derived base maps, environmental controls, and integrated mapping procedures. *International Journal of Remote Sensing*, *23*, 4551−4570.

Wheeler, J. O., Hoffman, P. F., Card, K. D., Davidson, A., Sanford, B. V., Okulitch, A. V., et al. (1997). *Geological map of Canada.* Geological Survey of Canada, Map D1860A.

Wu, C., & Murray, A. T. (2005). Estimating impervious surface distribution by spectral mixture analysis. *Remote Sensing of Environment*, *84*, 493−505.

Zhang, J., Rivard, B., & Sanchez-Azofeifa, A. (2005). Spectral unmixing of normalized reflectance data for the deconvolution of lichen and rock mixtures. *Remote Sensing of Environment*, *95*, 57−66.